nature communications

Article

https://doi.org/10.1038/s41467-025-58278-4

Catechol-based chemistry for hypoglycemia-responsive delivery of zinc-glucagon via hydrogel-based microneedle patch technology

Received: 5 September 2023

Accepted: 17 March 2025

Published online: 01 April 2025

Check for updates

Amin GhavamiNejad[1,3], Jackie Fule Liu[1,3], Sako Mirzaie[1,3], Brian Lu[1], Melisa Samarikhalaj[2], Adria Giacca[2] & Xiao Yu Wu[1]

Hypoglycemia is a serious and potentially life-threatening condition for people with insulin-dependent diabetes. To provide a safeguard against hypoglycemia, we introduce a "smart" microneedle (MN) patch that senses glucose levels and delivers a blood glucose-raising agent (Zinc-Glucagon (Z-GCN)) in response to hypoglycemia. Herein, we describe the use of catechol and boronic acid chemistry to design a self-crosslinkable hydrogel-based MN that stimulates the release of Z-GCN during hypoglycemia. In this design, the catechol groups bind to Z-GCN through metal-ligand complexation. At hyperglycemia, boronic acids react with glucose to generate cyclic boronate esters. As the glucose concentration decreases, the boronic acid groups dissociate and are favored over Z-GCN in binding with catechol, which promotes the release of Z-GCN. We fully characterize the fabricated MN in vitro. Moreover, we further evaluate the MN and demonstrate the in vivo glucose-responsive delivery of Z-GCN from the patch. We also show its effectiveness in preventing hypoglycemia for up to 6 h in type 1 diabetic male rats against two consecutive insulin overdose challenges. Since many proteins/peptides have a high binding affinity to metal ions, the introduced mechanism driven by the competitive binding of catechol-metal ions has great implications in drug delivery applications of various protein/peptide-based therapeutics.

Hypoglycemia or the state of abnormally low blood glucose levels ($\leq$ 70 mg/dL) is the most serious acute complication associated with insulin therapy that can result in death if left untreated[1]. Hypoglycemia is currently treated by rescue/emergency glucagon kits or nasal powder spray[2]. However, such emergency/rescue treatments still require someone to assist the patient and thus, are not ideal for patients who suffer from hypoglycemia unawareness or those under severe hypoglycemia who are alone, juvenile, elderly, confused, or unconscious. Hence, there is a clear need for preventative hypoglycemia therapies.

To date, two strategies have been employed to reduce the risk of hypoglycemia, including the use of glucose-responsive insulin analogs[3] and systems that deliver insulin, glucagon, and its derivatives glucose-responsively[4]. Glucose-responsive insulin analogs have not yet passed clinical trials due in part to the possibility of non-specific binding (other than the receptor) of the formulated insulin analogs[5]. Many

[1]Advanced Pharmaceutics and Drug Delivery Laboratory, Leslie L. Dan Faculty of Pharmacy, University of Toronto, Toronto, ON, Canada. [2]Departments of Physiology and Medicine, Institute of Medical Science and Banting and Best Diabetes Centre, Faculty of Medicine, University of Toronto, Toronto, ON, Canada. [3]These authors contributed equally: Amin GhavamiNejad, Jackie Fule Liu, Sako Mirzaie. e-mail: sxy.wu@utoronto.ca

glucose-responsive insulin[6,7] and glucagon delivery systems[8–12] have also been attempted via microneedle patches (MNs) and electro-mechanical closed-loop systems as well, but without much clinical success[13,14]. Most chemically-driven glucose-responsive drug delivery systems have used either concanavalin A (ConA)[15,16], glucose oxidase (GOX)[17–19], or phenylboronic acid (PBA)[20–23], as the glucose-sensing component. However, various hurdles, such as design complexity, complicated manufacturing processes, loss of the bioactivity of loaded drugs, and slow reaction response rate limited the application of these approaches[24].

Dynamic metal-ligand complexation has attracted significant interest in both fundamental and applied material science. The dynamic binding interactions could instantly dissociate, exchange, and reform[25]. Therefore, they can be used in designing "smart" materials with reversible "ON/OFF" bindings[26,27]. Currently, hydrogels formed by catechol-mediated reversible binding are under development for a wide range of applications[28–30]. Catechols are known to form reversible complexes with metal ions, metalloproteins, and boron-containing molecules, with the binding affinity being dependent on the nature of the molecules[31,32]. For instance, the catechol groups exhibit high specific affinities for iron, copper, cobalt, and relatively lower affinity for calcium and zinc[33–35]. Catechol-metal complexation is reversible and can be broken in the presence of a molecule with a higher affinity binding constant[36–39]. Boronic acid-containing monomers are an additional class of molecule which can form complexes with catechol groups[40,41]. However, these interactions can be influenced by glucose molecules in a competitive manner[42,43]. At high glucose concentrations, boronic acids react with glucose molecules to generate cyclic boronate esters. As the glucose concentration decreases, the boronic acid derivatives dissociate and bind competitively with catechol groups. In this scenario, if the catechol groups pre-chelated with a metal-containing molecule that has a lower affinity binding constant than boronic acid, the boronic acid will replace the metal-containing compound. It is also known that glucagon has inherent properties for interaction with metal ions (e.g., zinc)[44]. Previously, zinc-glucagon
(Z-GCN) was successfully used in the management of a male infant with persistent idiopathic hypoglycemia[45] and children with idiopathic infantile hypoglycemia[46]. Interestingly, it has been found that Z-GCN induces more prolonged effects than native glucagon in maintaining euglycemia in insulin-treated people with type 1 diabetes (T1D)[47].

In this work, we proposed to use the catechol-boronic acid-based chemistry and metal-catechol coordination chemistry to design a closed-loop self-crosslinked hydrogel-based MN patch using dopamine (DA) and 4-amino-3-fluorophenylboronic acid (AFBA)-functionalized hyaluronic acid (HA)-based polymers. The synthesized copolymers can deliver a blood glucose-raising agent (Z-GCN) at low glucose levels via a competitive binding between catechol-boronic and catechol-zinc to prevent the onset of hypoglycemia (Fig. 1). This design and release mechanism for Z-GCN delivery significantly distinct from previous studies on catechol-boronic acid-based microneedles that used glucose-induced swelling for insulin delivery at hyperglycemia[48]. In this design, at high glucose concentrations, the AFBA functional groups reversibly bind with glucose to generate cyclic boronate esters.

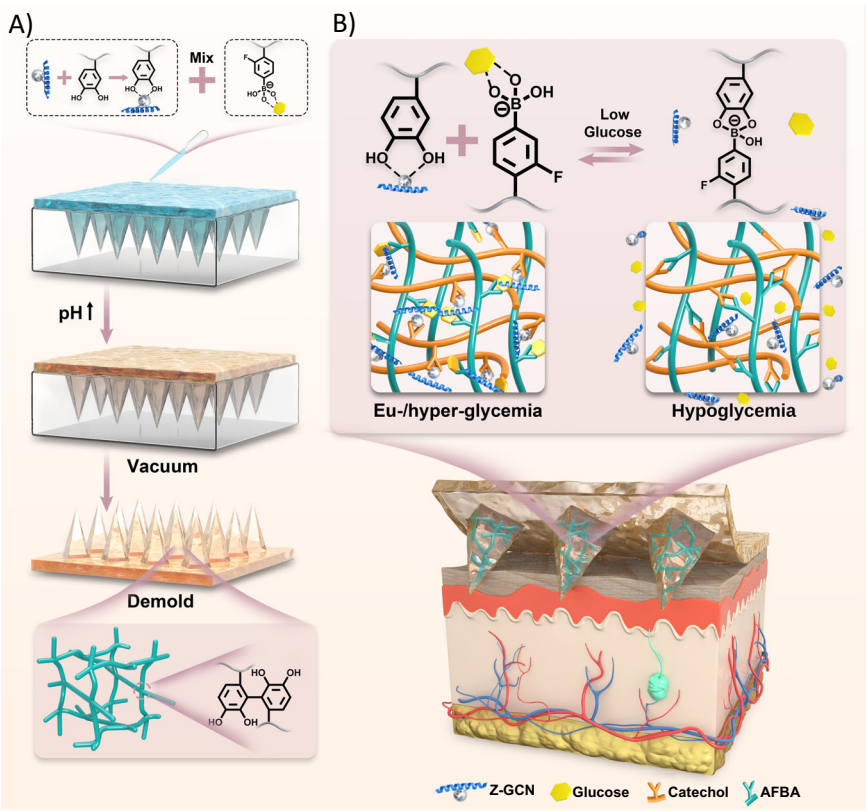

Fig. 1 | Overview of microneedle fabrication and glucose-responsive glucagon delivery mechanism. A Fabrication of the self-crosslinkable MN patch by utilizing the oxidation of catechol groups to the quinone structure and establishing irreversible catechol-catechol linkages. The color of hydrogel evolved from initially transparent to brown due to the catechol oxidation at elevated pH under slightly alkaline conditions. **B** After applying the patch, the MN penetrate through the stratum corneum and epidermis, swells quickly due to the diffusion of interstitial fluid, and enables the glucose responsive moieties of MN to be in contact with glucose. At hyperglycemia, the AFBA functional groups reversibly bind with glucose to generate cyclic boronate esters. Meanwhile, the catechol functional groups bind to Z-GCN through a metal-ligand complexation. At hypoglycemia, the AFBA is favored over Z-GCN in binding with catechol, which promotes the release of Z-GCN at low glucose concentrations.

Meanwhile, the catechol functional groups of DA bind to Z-GCN through a metal-ligand complexation. However, as the glucose concentration decreases, the AFBA will be favored over Z-GCN in binding with DA, due to its higher binding affinity and its free energy value, as confirmed by molecular dynamics (MD) simulations and quantum mechanics (QM) computations, which promotes the release of Z-GCN at low glucose concentration. We have fully characterized the MN patch in vitro and demonstrated its effectiveness in preventing hypoglycemia, against two consecutive insulin overdose challenges in vivo. The ability of this system to provide glucose-responsive glucagon delivery has the potential to enhance hypoglycemia management by shifting from reactive treatment to a proactive, preventive approach. This advancement could significantly reduce risks associated with insulin therapy, improve patient adherence, and offer greater reassurance to both patients and caregivers. Furthermore, it is well known that many proteins and peptides have a high binding affinity to metal ions, and almost half of all known proteins require metal ions to maintain their structures and biological functions. Hence, we believe that the introduced glucose responsive mechanism driven by the competitive binding of catechol-metal ions, is of great potential for protein/peptide drug delivery.

Results

Synthesis of polymers

Catechol- and boronic acid-containing copolymers were prepared by functionalizing HA (MW = 300 KDa) with various ratios of DA and AFBA (Tables S1 and S2). The successful introduction of DA and AFBA onto the HA backbone and their degree of conjugation were analyzed by ^{1}H-nuclear magnetic resonance (^{1}H-NMR) (Fig. S1). Mixing 5% (w/v) solutions of HA-DA with HA-AFBA at various mixing ratios (HA-DA: HA-AFBA = 1:1, 1:2, 1:3 (w/w)) at pH 8 gave rise to a three-dimensional polymeric network and subsequent gel formation, as confirmed by the successful completion of a tube inversion test (Fig. S2). The rheological analysis revealed that the storage modulus exceeds the loss modulus in all samples, suggesting a prevalence of solid-like behavior in the rheological profile of the gels (Fig. S3). Notably, within the frequency range of 0.1 to 100 rad/s, the storage modulus exhibits a progressive increase over time, attributed to the pronounced elasticity of the hydrogels formed via catechol-boronic acid binding. The driving force of gelation was due to the well-established reversible binding between boronic acid functionality of AFBA with catechol groups and irreversible catechol-catechol covalent crosslinking of oxidized catechol groups in the presence of oxygen. This dual crosslinking approach was validated using attenuated total reflectance—Fourier transform infrared (ATR-FTIR) spectroscopy (Fig. S4). The FTIR spectrum of polymers post-crosslinking exhibits a distinctive peak at 1480 cm^{-1}, indicative of catechol-boron complex formation. Additionally, a notable decrease in the broadband intensity of hydroxyl groups associated with catechol at ~3300–3400 cm^{-1} suggests the establishment of covalent catechol-catechol linkages.

Fabrication and characterization of MNs

A self-crosslinkable hydrogel-based MN patch was successfully fabricated using a 2 to 1 ratio of HA-DA to HA-AFBA. This ratio was selected due to the more efficient process of transferring the hydrogel precursor into the MN molds. For the MN patch fabrication, 1 mL HA-AFBA solution (50 mg/mL) containing 4 mg of glucose was mixed with 2 mL HA-DA solution (50 mg/mL) containing 3 mg of Z-GCN. This stock solution was then used to prepare 3 patches. The pH of the mixture was increased to 8, and then 1/3 of the total solution was added onto the MN mold, vacuumed, and dried at room temperature overnight. The MN had 100 % (1 mg) Z-CGN encapsulation efficiency due to the direct addition of Z-CGN into the matrix of MN. After complete desiccation, the MN patches were carefully separated from the mold and trimmed. The fabricated MN patch was arranged in a 10 × 10 array with MN tips with 800 µm in length (Fig. 2A, B). The mechanical compression testing of the MN patch demonstrated a force-at-break of 0.45 N per needle (Fig. 2C), which has sufficient strength for penetration into the rat's skin[9]. The mechanical properties of MNs were not significantly affected by gamma irradiation (25 kGy), and the sterilized MNs retained native sharpness. Scanning electron microscopy (SEM) images of the freeze-dried MN patches revealed the micron-size porosity in the internal structures of hydrogel that may provide an excellent environment for the diffusion of interstitial fluids (Fig. 2D). The swelling ratio of the patch was assessed by immersing the patches in pH 7.4 phosphate-buffered saline (PBS) (Fig. 2E). The MN patch exhibited a rapid super swelling behavior due to its porous structure with maximum swelling occurring at ~60 min while the needle array remained intact. The conjugation of DA to HA was also found to significantly increase the tissue adhesiveness of the patch. As shown in Fig. 2F, the adhesive stress of the hydrogel was significantly greater than non-catecholic hydrogels. It should be mentioned that MNs swelling during the application of hydrogel-based MN patches may weaken the adhesiveness of the hydrogels. However, the strong adhesive property of catechol groups under wet conditions provided a beneficial adhesion property to this patch. This is due to the interactions of the catechol groups with the thiol or amine groups of the skin surface[49].

In vitro glucose-responsive performance

To elucidate the competitive binding between boronic acids and catechol groups to interact with glucose and Z-GCN, the changes in the UV-Vis spectra of HA-DA in the absence and presence of glucose and Z-GCN were studied (Fig. 3A). The UV-Vis spectrum of the pure HA-DA revealed a peak at 280 nm representing the catechol groups of polymers[27]. The addition of Z-GCN to HA-DA showed a new peak at ~360 nm, indicating the formation of zinc-catechol mono-complexation[33]. Similarly, the addition of AFBA to HA-DA polymer solution showed a new peak around 470 nm related to the formation of boron-catechol complexation[27]. However, when both Z-GCN and AFBA were added to the HA-DA solution, the UV-Vis spectra only revealed a peak related to the AFBA-catechol binding, confirming that the interaction between catechol-boron is more pronounced than catechol-Z-GCN. The opposite trend was seen for this sample in the presence of glucose (70 mg/dL), where only the peak related to the interaction between Z-GCN and catechol could be observed, indicating that in the presence of glucose, glucose will be favored over catechol in binding with boronic acid. The suggested mechanisms in the hyper- and hypo-glycemic conditions have been illustrated in Fig. 3B.

QM modeling was further employed to elucidate the possible replacement of Z-GCN in the Z-GCN-catechol complex by boronic acid (AFBA) at a low concentration of glucose (Figs. 3C and S5). We studied the reaction energy profile of Zn-catechol and glucose-AFBA complexes as reactants and zinc ion, glucose, and AFBA-catechol as the products. The thermodynamic analysis showed that AFBA-catechol is the favored primary product, with a Gibbs free energy of −518.23 kcal/mol. Radial distribution function (RDF) data confirmed a strong interaction between the zinc ion and residue Phe 6 of GCN in a 100 ns MD simulation (Fig. 3D). Phe-Zn-catechol was used as a surrogate model for Z-GCN, replacing Zn-catechol in the second QM simulation run (Fig. 3E). This change supported earlier results, confirming the primary product's thermodynamic favoring with a Gibbs free energy of −600.67 kcal/mol. Cluster analysis of MD trajectories further disclosed the interaction mode between the zinc ion, GCN, and the polymer. To identify the predominant conformational states of the Z-GCN and polymer residues, we performed root mean square deviation (RMSD)-based cluster analysis on the MD trajectories. This approach enables us to group similar structural conformations throughout the simulation into distinct clusters, helping to capture the structural evolution of the complex over

https://doi.org/10.1038/s41467-025-58278-4

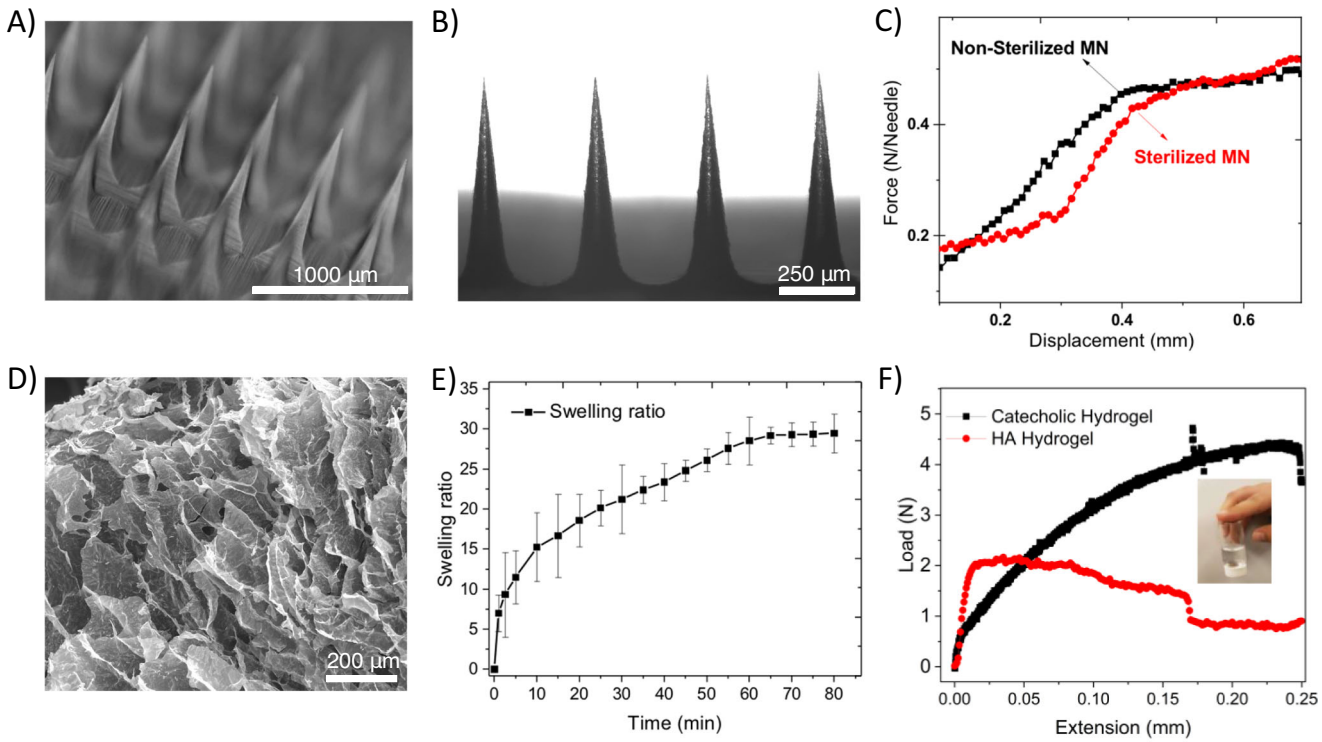

Fig. 2 | Characterization of the MN materials. A, **B** Transmittance microscopic images of microneedle array from different angles. **C** Mechanical compression strength of the MN patch before and after sterilization by gamma irradiation. A compressive force in the longitudinal direction of the MNs was generated at a speed of 0.5 mm/min. **D** SEM image showing the inner morphology and porosity of the fabricated patch. Scale bar = 200 μm. **E** Swelling ratio of the MN patch after immersing in PBS solution. ($n = 3$ independent samples, mean ± SD). **F** The force-displacement curves of adhesion of the synthesized hydrogel to the glass slides coated with a medical tape to mimic skin-like texture; inset shows a photograph of the hydrogel adhered to the skin of the finger.

time. Each cluster represents a unique conformational state, with the most frequent structural motifs corresponding to the largest clusters. By analyzing these clusters, we can determine the dominant conformations adopted by the system during the simulation, providing insight into the stability and flexibility of both the Z-GCN and polymer components. As shown in Fig. 3F, the zinc ion coordinates with both HA from the polymer and GCN's residue Phe 6 and interacts with three water molecules. The key role of Phe 6 in receptor recognition is known[50]. Density functional theory was used to study the catechol-AFBA complex formation, focusing on the highest occupied molecular orbital (HOMO), the lowest unoccupied molecular orbital (LUMO), and the energy gap (ΔE) (Fig. 3G). In the examined reaction, the Phe Zn in the Phe-Zn-catechol complex is replaced by AFBA, leading to the formation of AFBA-bound catechol. The process is characterized by a HOMO energy of −0.173495 eV and a LUMO energy of −0.065175 eV. This indicates that Phe Zn-bound catechol acts as an electrophile, with increased reactivity due to a lower energy gap (0.10832 eV)[51]. Conversely, glucose-bound AFBA, with HOMO and LUMO energies of −0.187550 eV and 0.009338 eV, respectively, serves as a nucleophile. The reaction progresses through a nucleophilic attack by glucose-bound AFBA on Phe Zn-bound catechol, causing the displacement of the Zn-bound Phe and releasing glucose. AFBA then binds to catechol to produce the thermodynamically favored product, catechol-bound AFBA. This comprehensive analysis, grounded in HOMO and LUMO energetics, unveils the intricate molecular interactions that drive this transformation. It not only validates the thermodynamic feasibility of forming catechol-bound AFBA but also emphasizes the orchestrated interplay between nucleophilic and electrophilic behaviors in the reactants. Such understanding augments our knowledge of this complex reaction pathway and potentially opens avenues for further exploration and application.

The glucose-responsive release of Z-GCN from the MN patch was determined in PBS buffer containing different glucose concentrations. Approximately 52% (0.52 mg) and 26% (0.26 mg) of the loaded Z-GCN were released after 45 min in media containing 50 and 70 mg/dL of glucose, respectively (Fig. 4A). It is worth noting that the targeted therapeutic dose for hypoglycemia rescue treatment is 1 mg of glucagon for adults and 0.5 mg for children weighing below 25 kg[52]. Therefore, the observed amount of drug released from the patch falls within the therapeutic target. Compared with the release rate of Z-CGN at hypoglycemic state, the preloaded Z-GCN showed significantly slower release at hyperglycemia with about 5% of the loaded Z-CGN released to the media. Such a minimal drug release indicates that the Z-GCN was tightly bound to the catechol groups, and its delivery profile is independent of volume changes of the MN that occur during the swelling. The repeated "ON/OFF" pulsatile release profile of Z-GCN from the patch was also carried out by immersing Z-GCN-loaded MNs in the media at different glucose concentrations (Fig. 4B). The results indicated a cyclic profile with a controllable Z-GCN release at various glucose concentrations, making it a safe and controllable drug delivery system. Far-UV Circular Dichroism (CD) spectropolarimetry was used to evaluate the stability of the Z-GCN and released Z-GCN from the MN patch, and the result was compared to native glucagon (Fig. 4C). The CD spectra of Z-GCN showed two similar peaks with native glucagon, which is predominantly attributed to the alpha-helix of this peptide. The CD spectra of released Z-GCN from the MN patch remained the same as freshly prepared glucagon, suggesting that the secondary structure of glucagon was preserved during zinc coordination, MN fabrication, and release study. To better quantify the changes in secondary structure fractions, deconvolution of the spectra was performed using the SELCON3 algorithm within the CDPro software. From deconvolution, it was found that native glucagon had 58.9% alpha-

https://doi.org/10.1038/s41467-025-58278-4

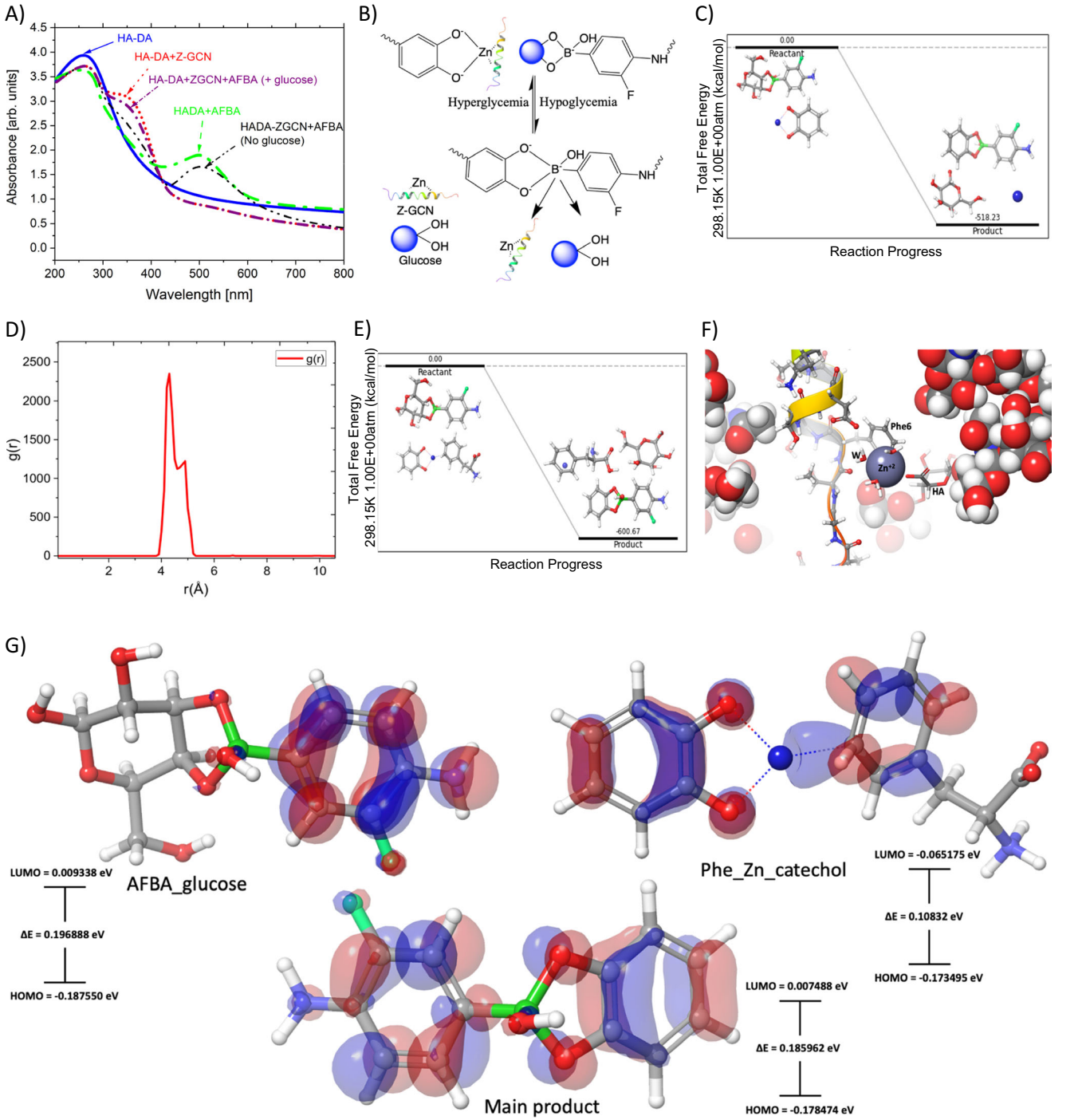

Fig. 3 | In vitro characterization and drug delivery mechanism of the MN materials. A UV-Vis spectra of HA-DA, HA-DA + Z-GCN, HA-DA + AFBA, and HA-DA + Z-GCN + AFBA in the presence and absence of glucose. **B** A schematic illustration of the Z-GCN, catechol and AFBA interactions in the presence of high/low glucose concentrations. **C** Reaction energy profile of reactants (Zn-catechol and glucose-AFBA complexes) and products (zinc ion, glucose, and AFBA-catechol). **D** Radial distribution function (RDF) as a function of distance between zinc ion and Phe 6 from GCN. **E** Reaction energy profile of reactants (Phe-Zn-catechol and glucose-AFBA complexes) and products (Phe-Zn, glucose, and AFBA-catechol). **F** Depiction of the interaction mode among zinc ion, solvent molecules, polymer, and GCN. In this illustration, the water molecules are denoted by 'W.' Interacting residues are represented using a stick model, while the non-interacting portions of the polymer and glucagon are shown through a ball model and cartoon presentation, respectively. **G** The density surface plots for the highest occupied molecular orbital (HOMO) and lowest unoccupied molecular orbital (LUMO) of glucose-AFBA, Phe-Zn-catechol, and catechol-bound AFBA.

helical content (Fig. 4D). Z-GCN and released Z-GCN retained 57.8 and 54.2% alpha-helical content, respectively.

Figure 4E, obtained from the cluster analysis of our computational data, suggests the interaction mode between Z-GCN and the polymer, revealing a multifaceted network of molecular associations. Within this complex, the guanidinium group of Arg 18 from Z-GCN forms two hydrogen bonds with the carbonyl moiety of HA-AFBA, contributing to the stability of the complex. Concurrently, Tyr 10 establishes a hydrogen bond with the HA moiety of the polymer, enhancing the specific interaction between Z-GCN and the polymer. Additionally, the imidazole ring of His 1 from Z-GCN engages in interactions with two HA residues from the polymer, while the amino group of His 1 further

https://doi.org/10.1038/s41467-025-58278-4

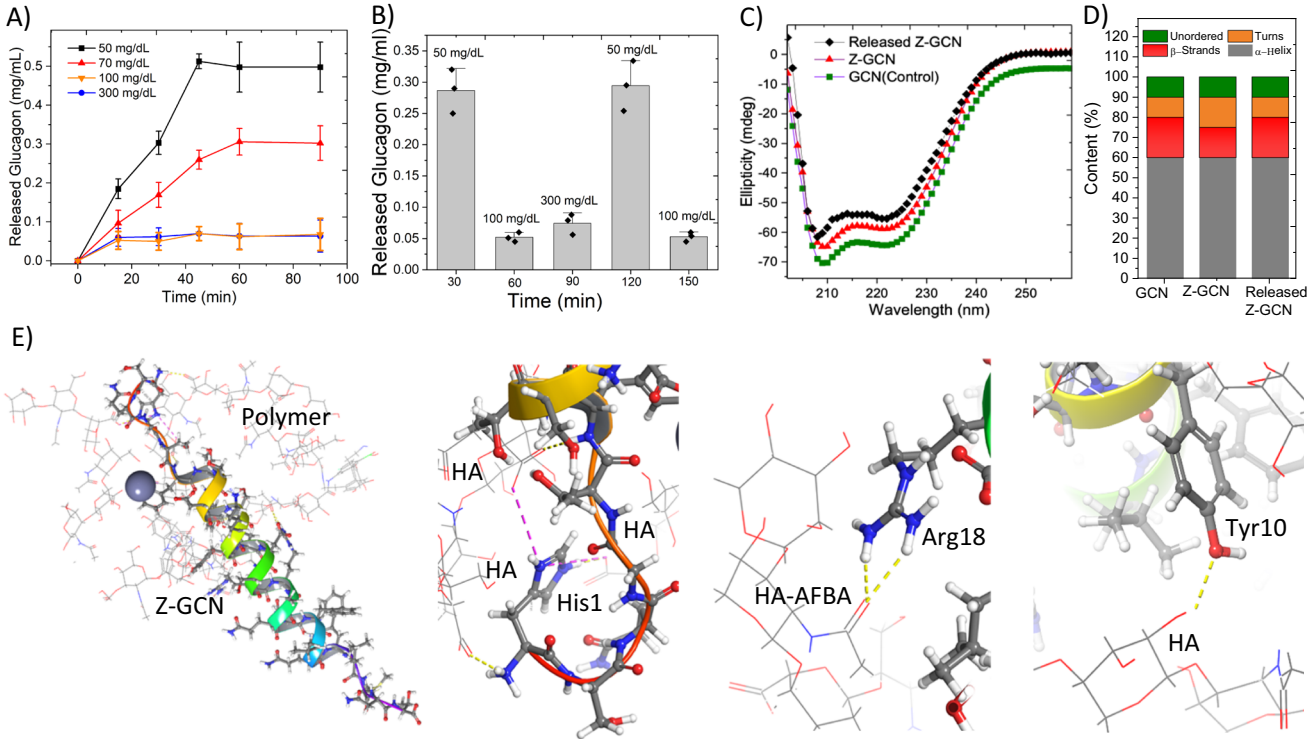

Fig. 4 | In vitro drug delivery characterization of MN and stability of the released drug. A In vitro glucose-responsive release of Z-GCN from the MN patch in PBS mimicking hypoglycemia (50 mg/dL), euglycemia (100 mg/dL) or hyperglycemia (300 mg/dL) ($n = 3$ independent samples, mean ± SD). **B** Pulsatile release of Z-GCN from the MN patch in varying glucose media (50, 100 and 300 mg/dL) ($n = 3$ independent samples, mean ± SD). **C** CD spectra of native glucagon solution and released Z-GCN. **D** The deconvolution of CD spectra to reveal fractions of glucagon secondary structure. **E** The calculated interaction mode between Z-GCN and the polymer, as determined by clustering analysis. Z-GCN and polymer residues are shown as ball-and-stick model and wire representation.

creates a hydrogen bond with the polymer (Fig. 4E). These intricate interactions collectively illustrate the structural basis underlying the association between Z-GCN and the polymer, offering insight into their potential functional interplay.

Molecular dynamic modeling

Examining the conformational space of complex systems like biological polymers is challenging due to high-energy barriers leading to rare transitions between energy minima. This often results in entrapment in these minima, creating quasi-ergodic behavior where parts of the system seem isolated. Understanding this landscape is vital for grasping the dynamics and functions of these macromolecules but remains a difficult problem to navigate[53]. Several strategies, including advanced statistical mechanical techniques like the multicanonical ensemble method[53–55], simulated tempering method[56], and parallel tempering or replica exchange method[53], have been devised to overcome quasi-ergodicity challenges in conformational space exploration for complex molecular systems. These methods collectively enhance sampling efficiency and accuracy, aiding a more profound understanding of system dynamics and structures. In this study, we utilized a tailored version of the replica exchange method, known as replica exchange with solute tempering (REST), specifically designed for efficiently exploring conformational space in aqueous biopolymer solutions.

In this study, two specific plots were generated to empirically demonstrate the adequacy of sampling in the investigation of the stabilizing mechanism of the polymer on Z-GCN (Fig. S6). We used REST for a comprehensive visual assessment of the sampling process of the Z-GCN alone (Fig. S6A) and Z-GCN in the presence of the polymer (Fig. S6B). These graphical representations serve a crucial function in verifying the sufficiency of sampling, confirming that the explored conformational space is adequately diverse and representative. The REST simulation in this study methodically explored interactions between Z-GCN and polymers and the polymer's stabilizing mechanism on glucagon's native structure. Timelines for all 10 replicas, presented in Fig. S7 and Table S4, revealed temperature-dependent changes in GCN's secondary structure and the polymer's modulatory role. Specifically, increasing the temperature from 300 to 481 K led to a reduction in the alpha-helix content of free GCN from 56.01% to 21.79%. This change indicates a temperature-induced perturbation in the peptide's conformation, reflecting the complexity of thermal responsiveness within its structure and emphasizing the polymer's role in this dynamic process.

Temporal snapshots of the Z-GCN both in the absence and presence of a polymer revealed significant structural insights (Figs. S8 and S9). Without the polymer, Z-GCN's helical structure distorts over time, indicating instability. In contrast, the polymer's presence remarkably preserves the alpha-helical structure (Fig. S9) thanks to interactions between the two (Fig. 4E). The polymer displays significant conformational flexibility and undergoes continuous reorganization throughout the simulation. This increased flexibility aligns with the findings of Taweechat et al., who observed that larger HA chains (HA20–HA50) exhibit higher conformational fluctuations[57]. Such flexibility is characteristic of HA-based polymers, allowing them to dynamically reorganize and adapt to their environment, enhancing their encapsulation and interaction capabilities.

An analysis of the RMSD values shows increased stability in the peptide-polymer complex, with the average RMSD of Z-GCN attenuated from 5.57 to 3.33 Å, indicating the increased stability in peptide-polymer complex (Fig. 5A). The root mean square fluctuation (RMSF) of Z-GCN residues was also lowered in the complex state (Fig. 5B), signifying sensitivity to the polymer's presence. Further, hydrogen bonds were computed, reflecting a robust interplay between the polymer and Z-GCN (Fig. 5D), but without remarkable changes in the

https://doi.org/10.1038/s41467-025-58278-4

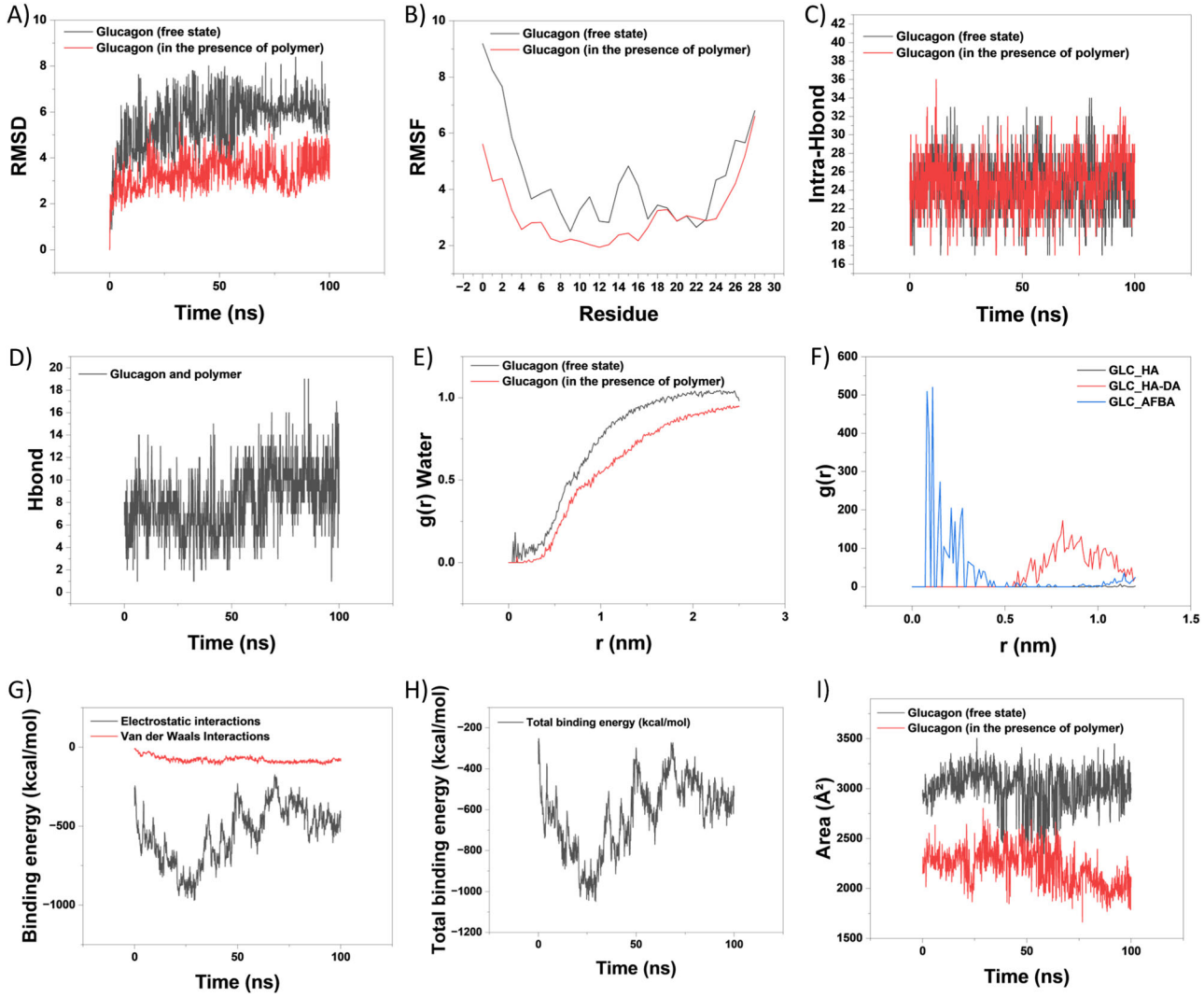

Fig. 5 | Results extracted from MD simulations of Z-GCN in the absence and presence of the polymer. A Z-GCN root mean square deviation (RMSD). **B** Z-GCN root mean-square fluctuation (RMSF). **C** Z-GCN intra-molecular H-bonding. **D** H-bonding between Z-GCN and polymer. **E** Radial distribution function (RDF) between water molecules and Z-GCN. **F** RDF between Z-GCN and polymer residues. **G** Electrostatic interaction and Van der Waals binding energies between Z-GCN and polymer. **H** Total binding energies between Z-GCN and polymer. **I** Solvent-accessible surface area (SASA) of Z-GCN in the absence and presence of the polymer.

intra H-bonding within glucagon (Fig. 5C). The RDF was used to analyze the spatial arrangement of water molecules around Z-GCN, revealing a pronounced shift in the hydration shell due to the polymer's influence (Fig. 5E). The RDF plot also illustrates a distinct pattern between Z-GCN and specific polymer residues, signifying preferential proximity between Z-GCN and the HA-DA residue (Fig. 5F). This suggests its role in influencing Z-GCN's orientation and stability within the polymer complex. The binding energy analysis reveals the predominance of electrostatic interactions, significantly overshadowing Van der Waals forces, in the overall binding affinity (Fig. 5G). These insights help to understand the specific manner of Z-GCN's engagement with the polymer (Fig. 5H). Finally, the solvent accessible surface area (SASA) analysis shows a marked decrease in Z-GCN 's SASA in the presence of the polymer (Fig. 5I). This reduction may reflect a conformational change or shielding effect by the polymer, altering Z-GCN's interaction dynamics with its surroundings. These comprehensive observations emphasize the critical role of the polymer in stabilizing the Z-GCN structure and provide an understanding of the complex molecular interplay between them.

Analysis of biocompatibility

Prior to the in vivo efficacy study, the biocompatibility and safety performance of MN patches were fully evaluated. First, the in vitro cytotoxicity of the MN patch was measured by performing MTT assay on HaCaT cells (Fig. 6A) (to mimic skin tissue) and NIH-3T3 fibroblast cells (Fig. S10). The results showed that the cell viability was not significantly influenced due to the high biocompatibility of the materials. The amounts of leachable and unreacted compounds from the patch were measured by reversed-phase high performance liquid chromatography (RP-HPLC) (Figs. 6B and S11). After 12 h of MN patch immersion in release media, only 0.0067 mg of DA and 0.002 mg of AFBA were detectable. Furthermore, the local biocompatibility of the MN patch was also evaluated via applying the patch onto the shaven dorsal region of rats and the tissue was analyzed after 7 days post-patch application (Fig. 6C). No microscopic tissue damage was observed across 7 days post-patch application. All three stains showed the presence of hair follicles, sebocyte lobules, and other cellular structures that are common to subcutaneous tissue morphology. Minimal presence of inflammatory markers (monocyte/macrophages)

https://doi.org/10.1038/s41467-025-58278-4

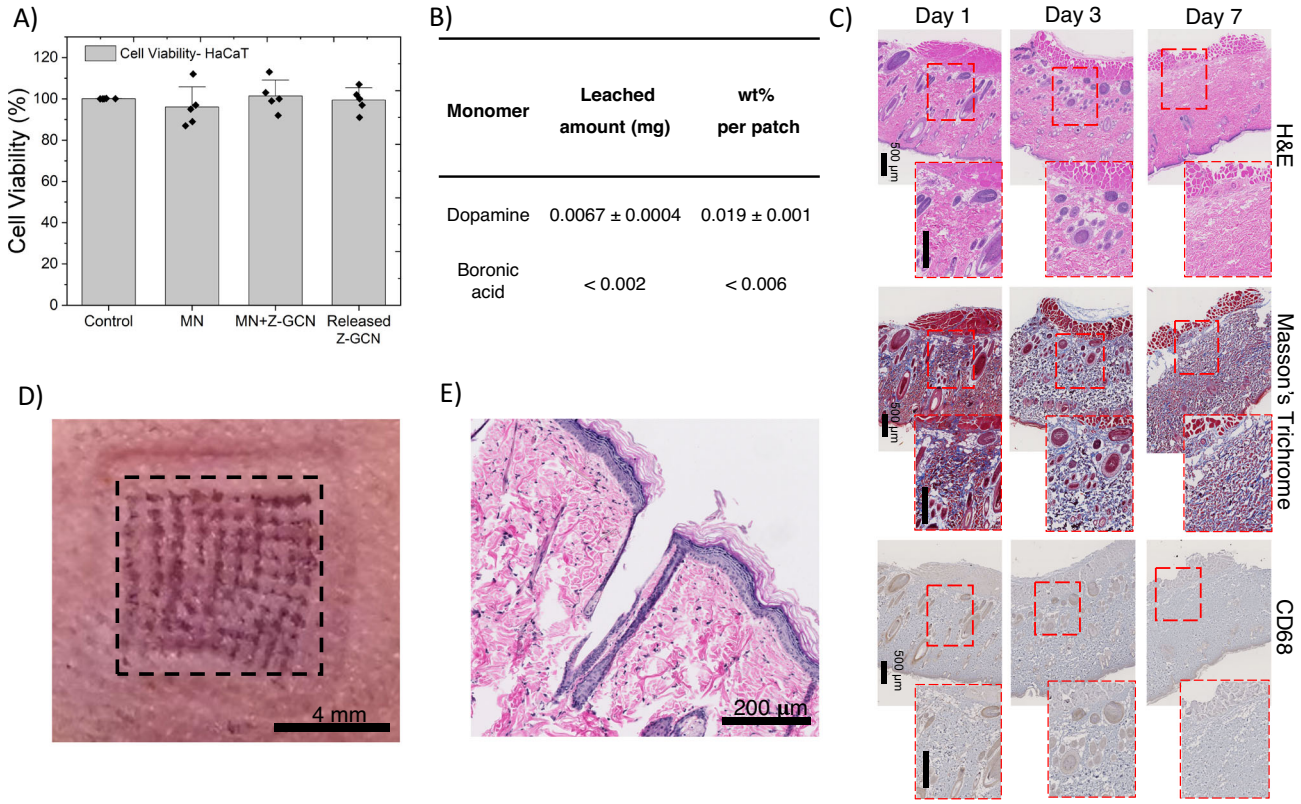

Fig. 6 | Safety assessment of MNs. A In vitro, cytotoxicity study of the MN, MN containing Z-GCN and released Z-GCN in HaCaT keratinocytes ($n = 5$ independent samples, mean ± SD). **B** The estimated amount of leachable comonomers released from the MN patch as detected by RP-HPLC. **C** Histological staining of rat skin up to 7 days post-patch application. The MN patch was applied on shaven rat skin for 12 h and removed thereafter. The treated area of the skin was excised one (day 1), three (day 3), and seven (day 7) days post-patch removal. Excised skin was stained with Hematoxylin and Eosin (H&E), Masson's Trichrome (MTC), and CD68 antibodies. Dashed red line boxes show an area with higher magnification, scale bars = 500 µm. No significant signs of skin inflammation were observed across seven days post-patch application. **D** Photograph and (**E**) histological analysis of H&E-stained tissue section of rat skin following Trypan blue dye loaded-MN insertion through the stratum corneum. Three biologically independent experiments were performed and representative result is shown.

was detected with CD68 staining over seven days after patch removal. Overall, the MN patch demonstrated no evidence of inducing tissue damage or inflammatory response and is thus, biocompatible.

In vivo hypoglycemia prevention

In vivo studies were evaluated in a streptozotocin (STZ, 65 mg/kg i.p.)-induced T1D rat model (male *Sprague Dawley* rats, Charles River). First, the MN skin penetration capability was tested in rats. MN loaded with blue dye was applied into the rat skin and removed after 15 min The MN patch provided sufficient strength for skin penetration, which was demonstrated on the shaven skin of a rat (Fig. 6D). This result was further confirmed by histological studies (Fig. 6E). After confirming the penetration capability of the device, the bioactivity of the Z-GCN was confirmed by subcutaneous administration in the T1D rats. As shown in Fig. 7A, the functionalized glucagon with 5% zinc did not significantly influence the bioactivity of glucagon. The increase in blood glucose levels after injection of glucagon and Z-GCN were maximal at 30 and 60 min, respectively. The duration of action of Z-GCN was found to be higher than glucagon. A similar phenomenon has been reported by others[47,58].

After confirming its bioactivity, we proceeded to test the hypoglycemia prevention capability of the MN patch in vivo against two insulin challenge overdoses, following the experimental design outlined in Fig. 7B. Rats were initially treated with the Z-GCN patch or a sham patch (control). Subsequently, the first and second insulin overdose injections (3 IU/kg each) were administered subcutaneously 30 min and 210 min post-patch application (Fig. 7B). Following the initial insulin challenge, rats with sham patches experienced a drop in blood glucose levels below the hypoglycemia threshold (70 mg/dL) within an hour, which continued to decline further by the end of the experiment. Some rats in the control groups even suffered seizures at the end of 6 h due to severe low blood glucose levels. Conversely, rats treated with the Z-GCN patch maintained their blood glucose levels above the hypoglycemia threshold during both insulin challenges, as shown in Fig. 7C. The comparison between the plasma glucagon levels of rats treated with the Z-GCN patch and sham patch was also demonstrated in Fig. 7D. At one-hour after application of the patches when the blood glucose level was still in the hyperglycemia range, the plasma glucagon levels remained at the basal value for both treatment groups, indicating no glucagon was released from the Z-GCN patch at hyperglycemia. However, when the blood glucose level reached the hypoglycemic range, a remarkable spike in plasma glucagon level was observed in the Z-GCN patch-treated group, whereas no significant change was detected in the sham patch-treated rats. Taken together, these results indicate that glucose-responsive Z-GCN release from the patch prevented hypoglycemia. To further confirm the glucose responsiveness of the patch, we conducted an additional experiment using the Z-GCN patch without insulin injection and compared it with a sham patch as a control. The results showed that like the shame patch, the Z-GCN patch did not raise the blood glucose level during hyperglycemia (Fig. 7E). These results confirmed the glucose-responsive delivery of Z-GCN from the MN patch and its ability to effectively prevent hypoglycemia for up to 6 h in T1D rats against two consecutive overdose insulin challenges.

Discussion

Here, we introduced a strategy to deliver a metal-containing blood glucose-raising agent in a glucose-responsive manner using catechol

https://doi.org/10.1038/s41467-025-58278-4

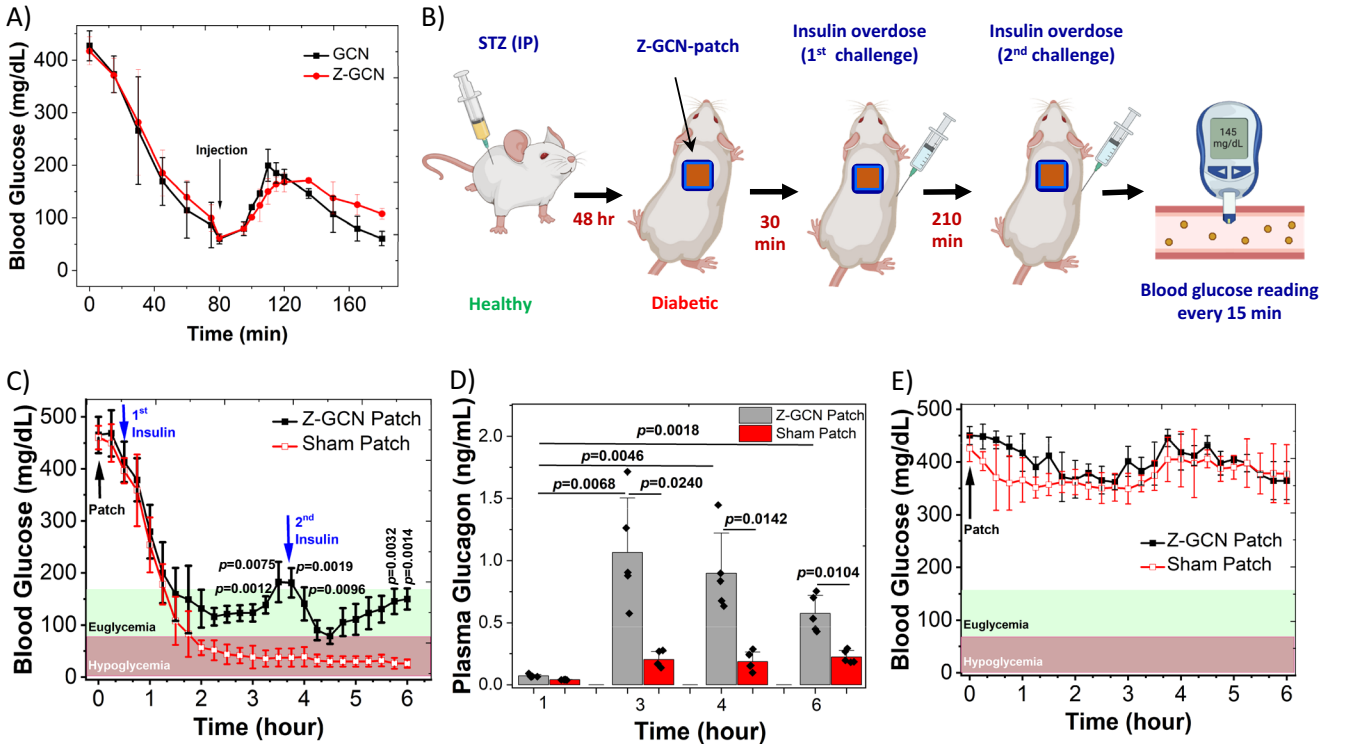

Fig. 7 | In vivo efficacy and hypoglycemia prevention study against two insulin overdoses in T1D rats. A The average blood glucose level of T1D rats after administration of 1 mg GCN vs 1 mg of Z-GCN ($n = 3$ biologically independent samples, mean ± SD). **B** In vivo study design of hypoglycemia prevention study. Created with BioRender.com/a84f160. **C** Average blood glucose levels in T1D rats vs. time following the application of the Z-GCN patch or sham patch at $t = 0$ during two cycles of insulin overdose injections. ($n = 5$ biologically independent samples, mean ± SD). Statistical significance was determined using a two-way repeated measure Analysis of Variance (ANOVA) with a Geisser–Greenhouse correction and Bonferroni post hoc test. **D** Plasma glucagon levels as determined by glucagon ELISA (indicated times are post-patch application). ($n = 5$ biologically independent samples, mean ± SD). The p-values and statistical significance were determined using two-sided Student's t-test. **E** Average blood glucose levels vs. time following the application of the Z-GCN patch or sham patch at $t = 0$ under hyperglycemia conditions. ($n = 3$ biologically independent samples, mean ± SD).

and boronic acid chemistry. We took advantage of the catechol-boronic acid binding to design a self-crosslinkable hydrogel-based MN patch for Z-GCN delivery at hypoglycemia. The MN patch is composed of catechol and boronic acid-functionalized HA-based polymers that can be self-crosslinked upon mixing the polymer solutions at pH 8. The self-crosslinking method of fabricating the MN patch enables a higher drug loading efficiency and the avoidance of using chemical cross-linkers, photoinitiators, and heating processes allowing the MN patch to preserve the stability of Z-GCN throughout the entire patch fabrication process, as confirmed by in vitro, in vivo, and all-atom molecular dynamics simulations. In this design, at high glucose concentrations, the AFBA functional groups reversibly bind with glucose to generate cyclic boronate esters. Meanwhile, the catechol functional groups bind to Z-GCN through a metal-ligand complexation. When the glucose concentration decreases, the AFBA is favored over Z-GCN in binding with catechol, due to its higher binding affinity and its free energy value, which promotes the release of Z-GCN at low glucose concentrations. We have further demonstrated the in vivo glucose-responsive delivery of Z-GCN from the patch and its effectiveness in preventing hypoglycemia for up to 6 h in T1D rats against two consecutive overdoses of insulin challenge. The capabilities offered by this system can shift the paradigm of hypoglycemia therapy away from an acute intervention towards a preventative approach, significantly de-risking insulin therapy, improving patient compliance, and providing security to both patients and their caregivers. Furthermore, a variety of drug delivery applications may be achieved by tuning/modification of the catechol-containing polymer architecture, composition, and metal-containing therapeutic proteins. As metal ions exist in many therapeutics as excipients or conjugates, this drug delivery strategy may provide a versatile approach for the delivery of various proteins and peptides to treat a broad range of diseases.

Methods

Materials

The pharma injection-grade sodium hyaluronic acid (HA, MW 300 kDa) was purchased from Bloomage Co., Ltd (China). All the chemicals were purchased from Sigma-Aldrich (USA) unless otherwise specified. Synthetic glucagon was purchased from Biomatik Corp. (Ontario, Canada). USP-grade human recombinant insulin (27 IU/mg) was purchased from Wisent (Quebec, Canada). HPLC-grade acetonitrile and water were purchased from Caledon Labs (Ontario, Canada). The distilled deionized (DDI) water was prepared from a Millipore Purification system. All reagents were of analytical grade or higher and were used without further purification.

Synthesis of HA-DA

HA-DA was synthesized by N-(3-dimethylaminopropyl)-N′-ethylcarbodiimide hydrochloride and N-hydroxy succinimide (EDC/NHS) coupling reaction. First, HA (1 g) was dissolved in DDI water (100 mL), and the mixture was kept under stirring overnight. NHS (1.5 mmol) and EDC (1.5 mmol) were added to the HA mixture at a 15-minute interval while stirring. In the next step, DA hydrochloride (1.6 mmol) was added to the solution. The pH of the solution was adjusted and maintained at 5.5 using 1 M hydrochloric acid, and the solution was kept under stirring for 12 h. In the next step, the product was dialyzed at room temperature using dialysis tubing cellulose membrane (MWCO 12–14 kDa, Spectrum™ Spectra/Por™) in DDI water (pH 6). The complete removal of free DA was confirmed by UV-vis spectroscopy. The purified product

was transferred to falcon tubes, freeze-dried, and stored at 4°C (yield: 96%). The chemical structures of HA-DA and HA-AFBA were characterized using ^{1}H-NMR in D_2O (400 MHz, MercuryPlus, Varian) and UV-vis spectroscopy. The degree of substitution of DA was calculated using UV-Vis and ^{1}H-NMR by the integral of the peak related to the N-acetyl group of HA at δ = 1.9–2.0 ppm to the aromatic peaks of DA at δ = 6.7–7.0 ppm.

Synthesis of HA-AFBA

Synthesis of HA-AFBA (4-amino-3-fluorophenylboronic acid) was similar to HA-DA. Instead of dissolving HA in DDI water, AFBA (0.6 mmol) was added to the HA mixture (50 mL) containing DDI water/ethanol (70/30 w/w). The HA-AFBA product was purified in DDI water and lyophilized for later use (yield: 80%). The degree of AFBA conjugation was determined to be around 12.9% using the ^{1}H-NMR spectrum by integration of the aromatic peaks of AFBA at δ = 7.5–8.0 ppm to the peak at δ = 1.9–2.0 ppm related to the N-acetyl glucosamine of HA.

Modification of glucagon with zinc (Z-GCN)

Z-GCN was made by suspending freeze-dried glucagon in a zinc acetate buffer for a final concentration of 1 mg glucagon/mL, 0.05 mg zinc/mL[59]. The secondary structure of the peptide was characterized before and after Zn-coordination/modification by CD spectropolarimetry.

Fabrication of MN patch

A self-crosslinkable polymer-based MN patch was successfully fabricated using a rationally selected ratio of HA-DA and HA-AFBA (2:1). First, 1 mL of HA-AFBA solution (50 mg/mL) containing 3 mg of glucose was mixed with 2 mL HA-DA solution (50 mg/mL) containing adequate amount of Z-GCN. Next, the pH of the mixture was adjusted to 8 using 1 M NaOH and stirred with a spatula until the color of the solution turned brown. Then the mixture was added into a polydimethylsiloxane (PDMS) MN mold and vacuumed under 25 mmHg for 5 min to remove trapped air. The mold was kept at room temperature in a fume hood overnight. After complete desiccation, the MN patches were carefully separated from the mold and trimmed.

Characterization of MN patch

The rheological properties of the hydrogels were tested using a a hybrid rheometer (Discovery HR3, TA instruments) with a 40 mm parallel plate geometry at 1 Hz. Attenuated total reflectance - Fourier transform infrared (ATR-FTIR) spectroscopy was conducted to study the bonding configuration of MNs. The IR spectra were recorded at room temperature using a Paragon 1000 spectrometer (Perkin Elmer) equipped with VeeMax II variable angle ATR accessory. Proton nuclear magnetic resonance (^{1}H-NMR) spectra were recorded in deuterated water (D_2O) with a MercuryPlus, Varian Spectrometer (400 MHz). The inner morphology of MNs was determined by scanning electron microscopy (SEM, Prisma™ E) at an acceleration voltage of 20 kV, and the dimension of the needles was determined by an inverted fluorescence microscope (IX 71, Olympus). The content of catechol and AFBA was determined using UV-Vis spectroscopy at 280 nm and 250 nm, respectively. UV-Vis analysis was carried out with a UV-Vis spectrometer using quartz cuvettes (1 cm path length). UV-Vis intensity values of the catechol and AFBA-modified polymers were correlated to the concentrations using standard curves generated from known concentrations of DA or AFBA solutions. The obtained values are slightly higher than those obtained from ^{1}H-NMR analysis, which may be attributed to variations in the molecular environment between the two methods. UV-Vis absorption was also studied for the interactions between HA-DA, AFBA and Z-GCN with and without glucose. To obtain higher resolution in the UV-Vis spectrum, we used only AFBA monomer instead of HA-AFBA.

Gamma-ray sterilization of MN patch

We have sterilized the MN patches using a gamma-ray irradiation facility at the University of Toronto to study the effect of sterilization on the mechanical properties of the patches. The equipment used for the gamma irradiation is the Gamma Cell, type G.C. 220. The Gamma Cell utilized an annular Co-60 source enclosed within a lead shield chamber. The MN patches were exposed to a total dose of 25 kGy in a sealed chamber with an evenly distributed gamma field for one week to render them sterile. The sterilized MN patches were observed under a microscope to check for the changes in the morphological characteristics.

CD spectropolarimetry

The secondary structure of glucagon and Z-GCN before and after release from the MN patch was examined using CD spectropolarimetry (Jasco J-810, MD, USA) within the far-UV wavelength range of 200–260 nm. Samples were prepared by diluting them in a pH 7.4 PBS solution containing glucagon solubilizer of MSB. The diluted samples were transferred into a quartz cuvette with 1 cm path length. Scans were performed at 1 nm intervals across the 200–260 nm range, with each data point recorded over an 8-second response time. Measurements were repeated four times and averaged results were obtained. The resulting spectra were compared to a freshly prepared glucagon standard (containing MSB solubilizer in pH 7.4 PBS). To estimate the fraction of peptide secondary structures, the SELCON3 algorithm from CDPro software (Colorado State University) was used for spectra deconvolution.

RP-HPLC

RP-HPLC was performed to assess the remaining protein content of Z-GCN released from MNs compared to freshly prepared glucagon standard solutions (containing MSB solubilizer, pH 7.4 PBS). Native glucagon and its potential degradation products were separated using a Kinetex C-18 column (2.6 µm 110 Å, 4.6 mm × 150 mm, Phenomenex, CA, USA). For each run, 40 µL of the sample was injected into the column and analyzed at a flow rate of 0.75 mL/min. The mobile phase consisted of solvent A (0.1% v/v TFA in water) and solvent B (0.1% v/v TFA in acetonitrile), with a linear gradient shifting from 72% A and 28% B to 47% A and 53% B over 15 min. Following each sample, the column was flushed with 72% A and 28% B for 10 min. The column was maintained at 34 °C (skin temperature) throughout the study. Glucagon and any degradation products were detected by monitoring their elution times at 220 nm using a UV detector.

Mechanical/adhesion strength of MNs

The mechanical strength of MN arrays was tested using Instron 3366 universal testing machine equipped with a compression cell. The MN arrays were placed vertically on a compression plate. The distance between the two plates was set to 2 mm. A compressive force was applied at a speed of 0.5 mm/min, with the compression threshold set to 10 N. Load (force; N) and displacement (distance; mm) were then recorded every 0.05 s to generate the load-displacement curve. For the measurement of hydrogel adhesion, lap shear joints were prepared, following a process frequently used for measuring the adhesive strength of hydrogel-based tissue adhesives. Two ribbons of hydrogels (length l × width w = 75 mm × 25 mm) were cut. They were brought into contact with two glass slides coated with a medical tape (melt-blown polyurethane) to mimic skin-like texture. The lap joint was slightly pressurized with a 20 g weight for 5 min, and then the two ends of the glass were clamped to the tensile machine. The shear adhesive test was conducted at a shear velocity of 100 mm/min under ambient conditions. The applied force and displacement were recorded.

Swelling studies

The swelling profile of the MN patch was assessed by immersing the patch in pH 7.4 PBS. The MN patch swelled rapidly upon immersing in PBS buffer. The net weight of the swelled MN patch was carefully measured at predetermined time points. The swelling ratio was calculated based on a formula of the weight of the MN patches at various times (W_t) to its initial net weight (W_0) as shown below.

$$Swelling\ Ratio\% = \frac{Wt - W_0}{W_0} \times 100 \quad (1)$$

Molecular dynamic simulation

For simulating the effect of HA-functionalized polymer on the stability of glucagon, a hormone molecule with the PDB ID of 1GCN was downloaded from the protein data bank[60]. Two distinct systems, one with glucagon alone and the other with glucagon in the presence of the polymer, were examined through molecular dynamics simulations using the Desmond software from Schrödinger Inc[61]. Based on the molar ratios determined from ^{1}H-NMR measurements, the proportions of disaccharides were set to 78% for HA, 16% for HA-DA, and 8% for HA-AFBA to construct a crosslinked polymer. Both systems, consisting of free glucagon or glucagon in complex with the polymer, were solvated using the explicit TIP3P water model[62] and the OPLS3 force field parameters[63]. For each MD simulation, the conditions were set to a temperature of 310 K, a pH of 7.4, and a pressure of 1 bar, with a total simulation time of 100 ns. Long-range electrostatic interactions were calculated using the particle-mesh Ewald method, while Coulomb interactions were evaluated within a 9.0 Å cut-off radius. A cubic periodic box with periodic boundary conditions was established for both systems during the solvation process[9]. To neutralize each system, Na^+ and Cl^- counterions were added. A 10.0 Å buffer distance was maintained between the periodic boundary conditions and the nearest atom of either free glucagon or the glucagon-polymer complex. For pressure and temperature regulation during the MD simulations, the Martyna–Tuckerman–Klein chain coupling scheme was applied for pressure control, while the Nosé–Hoover chain coupling scheme was used for temperature control[8]. A total of 1000 frames per MD run were generated, with trajectories recorded at 10 ps intervals. Following the equilibration of each system, Replica Exchange with Solute Tempering (REST) was performed[64]. For enhanced conformation sampling using REST, a total of 10 replicas were generated to be simultaneously simulated for 100 ns each at temperatures ranging from 300 K to 481 K. (Table S3). In REST, the total interaction energy of the system was divided into three components:

1. E_{pp}: the intramolecular energy of the Z-GCN /polymer
2. E_{pw}: the interaction energy between the Z-GCN /polymer and water
3. E_{ww}: the self-interaction energy of water molecules.

Replicas simulated at varying temperatures evolve under distinct Hamiltonians, where the three energy components are scaled accordingly. Specifically, the potential energy of a replica at temperature T_m is expressed as:

$$E_m^{REST}(X) = E_{pp}(X) + \frac{\beta_0 + \beta_m}{2\beta_m} E_{pw}(X) + \frac{\beta_0}{\beta_m} E_{ww}(X) \quad (2)$$

In this context, "X" represents the configuration of the entire system, while $\beta_m = 1/k_B T_m$, where T_0 denotes the reference temperature. At T_0, the potential energy simplifies to its standard form. By enforcing the detailed balance condition, the acceptance ratio for exchanging replicas m and n is determined by the following energy difference:

$$\Delta_{mn}(REST) = (\beta_m - \beta_n)[(E_{pp}(X_m) + \frac{1}{2}E_{pw}(X_n)) - (E_{pp}(X_m) + \frac{1}{2}E_{pw}(X_m)] \quad (3)$$

The water self-interaction energy, E_{ww}, is excluded from the acceptance ratio formula, allowing REST to achieve high exchange probabilities with a relatively small number of replicas[64].

QM computations

The Zn-catechol, glucose-AFBA, zinc ion, glucose, AFBA-catechol, and Zn-Phe-Zn-catechol were constructed with GaussView software[65]. For calculating the reaction energies of reactants and products, the density functional theory of B3LYP-D3 and the basis set of LACVP** were used. In all QM studies, water was selected as the solvent. Due to the presence of zinc, the geometries of the reactants and products were optimized with PCM (polarizable continuum model) and followed the single point energy calculation by PBF (Poisson Boltzmann Finite element) model. These methods ensure that solvent effects are fully considered, as they play a significant role in the reaction energies and overall stability of the system. All QM calculations were conducted using Jaguar[66].

In vitro release study

Glucose-responsive Z-GCN release from MN patches was determined in PBS buffer (pH 7.4) containing glucagon solubilizer, myristylsulfobetaine (MSB), and varying glucose concentrations (50, 70, 100, or 300 mg/dL). Vials were placed in a 34 °C incubator to mimic skin temperature. Drug release over time was measured using RP-HPLC. The pulsatile release profile of the MN patches was also analyzed by replacing the released media with different glucose concentrations.

In vitro cytotoxicity assay (evaluation of biocompatibility)

HaCaT cell line (human keratinocytes, cat. 116027) was purchased from Antibody Research Corporation (Missouri, USA). The in vitro cytotoxicity of the MN patch was measured by performing 3-(4,5)- dimethylthiahiazo(-z-y1)- 3,5-di phenytetrazoliumromide (MTT) assay on NIH3T3 fibroblast cells and HaCaT cells to mimic the skin. Briefly, cells were seeded at a density of 10000 cells per well in a 96-well plate in 200 µL of Dulbecco's Modified Eagle Medium (DMEM) with 10% fetal bovine growth serum (FBS). After incubation for 24 h at 37 °C, cells were treated with MN materials and incubated for an additional 24 h at 37 °C. The dosage of Z-GCN and MN materials was prepared according to the concentration required for fabricating the MN patch. In the next step, 100 µL of 10% SDS in 0.01 M HCl was added to each well and incubated for an additional 4 hours. The absorbance of the samples was measured using a UV plate reader (BioRad) at 570 nm. To calculate the cell viability for survival%, the following equation was applied and plotted on a semi-log scale.

$$\text{Survival\%} = \frac{\text{sample signal} - \text{background signal}}{\text{control signal} - \text{background signal}} \times 100 \quad (4)$$

Leachable compounds study

RP-HPLC/UV was used to separate, detect, and quantify the amount of leachable compounds (unreacted comonomers) released from the MN patch. An HPLC method was carefully developed to capture, separate with reasonable resolution, and quantify the compounds of interest. In brief, a ZORBAX Extend C-18 column (3.5 µm, 4.6 mm × 150 mm) was used with a gradient elution profile with water and methanol as the solvents of the mobile phase. The gradient was changed from 72% water/ 28% methanol at time zero to 47% water/ 53% methanol at

$t = 25$ min before returning to the original composition at $t = 30$ min. The column was set to 40 °C, the flow rate at 0.45 mL/min, and the detection wavelength at 220 nm. Leachable compounds from the MN patch were collected by immersing the whole patch in 5 mL of release buffer for 12 h. Concentrations of leachable compounds were extrapolated from a calibration curve generated by standards ranging from 0.1 to 0.006 mg/mL. Regression analysis was performed accordingly.

Animal experiments

All animal experiments were conducted in strict compliance with the ethical and legal regulations outlined in the Ontario Animals for Research Act and the guidelines provided by the Canadian Council on Animal Care. These procedures were approved by the University of Toronto's Animal Care Committee (Protocol #: 20011316). Male *Sprague Dawley* rats (Charles River) were administered STZ (65 mg/kg, i.p.) to induce a T1D model. The STZ-treated rats were closely observed for 1 week, with blood glucose levels measured every 2 days using a glucose meter (OneTouch® Ultra®, LifeScan, Inc., USA). Diabetic rats with stable blood glucose levels above 17 mmol/L were selected for the study. Before the experiment, the rats were fasted for 5 h to ensure the clearance of food from the gut and were grouped randomly.

In vivo skin penetration study

A trypan blue-loaded microneedle was applied onto the shaven back of the T1D rats for 15 min. Afterward, the patch was removed, and the treated skin was photographed. For histological analysis, the penetrated skin samples were fixed in 10 % buffered formalin for 24 h and embedded in paraffin. Samples were then sectioned into 5 mm thick slices and stained with hematoxylin & eosin (H&E).

Local (skin) biocompatibility study

To evaluate the local biocompatibility of the MN patch, the patch was applied onto the shaven dorsal region of STZ-induced T1D rats overnight (12 h) and removed. The patch-treated skin area was excised one-, three-, and seven-day post-patch removal. The excised tissues were immediately fixed in 10% buffered formalin for 48 h and transferred to 70% ethanol. The tissues were then sectioned and stained using H&E, Masson's trichrome (MTC), and CD68 antibodies (Abcam, ab125212). The stained sections were analyzed under high-resolution bright-field microscopy to observe for inflammatory markers and tissue damage. H&E-stained nuclei of cells are stained purple, and extracellular matrix/cytoplasm cells are stained pink. MTC is a stain for differentiating between cells and connective tissue: muscle fibers, keratin, and cytoplasm are stained red; nuclei are stained blue; and collagen is stained blue/green. CD68 stained for inflammatory markers such as monocytes/macrophages with a dark brown hue.

In vivo efficacy in T1D rats

In vivo studies were evaluated in an STZ-induced T1D model in male rats. The diabetic rats were fasted for 5 h to ensure the clearance of food from the gut. The rats were then anaesthetized by I.P. injection of ketamine and shaved and treated with hair removal cream before applying Z-GCN loaded MN patch or sham device (control) at $t = 0$. The first insulin challenge was carried out by subcutaneously injecting native insulin at a dose of 3 IU/kg. The blood glucose levels were monitored every 15 min for 3 h with a glucometer using a tail pricking/strip method. After a 3-hour treatment, another insulin solution at a dose of 3 IU/kg was given to the Z-GCN patch-treated group, and the blood glucose levels were monitored every 15 min up to 6 h. The rats that experienced seizures due to severe hypoglycemia received 50% dextrose injections (1 g/kg, i.p.) as a rescue treatment. Blood samples (250 µL per rat) were collected from the tail vein of rats at predetermined timepoints and centrifuged to isolate plasma, followed by storing at −20 °C until assay. Plasma glucagon level was measured using a Glucagon Quantikine ELISA kit (R&D System).

Statistical information

All data are expressed as mean ± standard deviation. All the statistical analysis for the in vitro studies was conducted using a two-tailed unpaired Student's t-test. Differences between experimental groups and control groups were considered statistically significant with a p-value < 0.05. Statistical significance between groups in the in vivo efficacy study was determined using a two-way repeated measure analysis of variance (ANOVA) with a Geisser–Greenhouse correction and Bonferroni post hoc test, performed using GraphPad Prism 9.0 software and OriginPro 2023. In the microscope experiments, three independent experiments were performed, and representative images were shown.

Reporting summary

Further information on research design is available in the Nature Portfolio Reporting Summary linked to this article.

Data availability

The main data supporting the results in this study are available within the paper and its Supplementary Information. All data underlying this study are available from the corresponding author upon request.

References

1. Perkins, B. A., Sherr, J. L. & Mathieu, C. Type 1 diabetes glycemic management: Insulin therapy, glucose monitoring, and automation. *Science* **373**, 522–527 (2021).
2. Patil, M., Deshmukh, N. J., Patel, M. & Sangle, G. V. Glucagon-based therapy: past, present and future. *Peptides* **127**, 170296 (2020).
3. Hoeg-Jensen, T. Review: glucose-sensitive insulin. *Mol. Metab.* **46**, 101107 (2020).
4. Wang, J. Q. et al. Glucose-responsive insulin and delivery systems: innovation and translation. *Adv. Mater.* **32**, e1902004 (2020).
5. Krug, A. W. et al. Clinical evaluation of MK-2640: an insulin analog with glucose-responsive properties. *Clin. Pharm. Ther.* **105**, 417–425 (2019).
6. Yu, J. C. et al. Glucose-responsive insulin patch for the regulation of blood glucose in mice and minipigs. *Nat. Biomed. Eng.* **4**, 499–506 (2020).
7. Zhang, Y. Q. et al. Advances in transdermal insulin delivery. *Adv. Drug Deliv. Rev.* **139**, 51–70 (2019).
8. Lu, B. et al. "Smart" composite microneedle patch stabilizes glucagon and prevents nocturnal hypoglycemia: experimental studies and molecular dynamics simulation. *ACS Appl Mater. Inter* **14**, 20576–20590 (2022).
9. GhavamiNejad, A. et al. Transdermal delivery of a somatostatin receptor type 2 antagonist using microneedle patch technology for hypoglycemia prevention. *Drug Deliv. Transl. Res.* **12**, 792–804 (2022).
10. GhavamiNejad, A. et al. Glucose-responsive composite microneedle patch for hypoglycemia-triggered delivery of native glucagon. *Adv. Mater.* **31**, e1901051 (2019).
11. Wang, Z. J. et al. Dual self-regulated delivery of insulin and glucagon by a hybrid patch. *Proc. Natl. Acad. Sci. USA* **117**, 29512–29517 (2020).
12. Yu, J. C. et al. Insulin-responsive glucagon delivery for prevention of hypoglycemia. *Small* **13** (2017).
13. Fuchs, J. & Hovorka, R. Benefits and challenges of current closed-loop technologies in children and young people with type 1 diabetes. *Front Pediatr.* **9**, 679484 (2021).
14. Leon-Vargas, F., Arango Oviedo, J. A. & Luna Wandurraga, H. J. Two decades of research in artificial pancreas: insights from a bibliometric analysis. *J. Diabetes Sci. Technol.* **16**, 434-445 (2021).
15. Hurkat, P. et al. Concanavalin A conjugated biodegradable nanoparticles for oral insulin delivery. *J. Nanopart. Res.* **14**, 1219 (2012).

16. Zhang, R., Tang, M., Bowyer, A., Eisenthal, R. & Hubble, J. Synthesis and characterization of a d-glucose sensitive hydrogel based on CM-dextran and concanavalin A. *React. Funct. Polym.* **66**, 757–767 (2006).
17. Li, J. et al. Microfabricated microporous membranes reduce the host immune response and prolong the functional lifetime of a closed-loop insulin delivery implant in a type 1 diabetic rat model. *Biomaterials* **47**, 51–61 (2015).
18. Gordijo, C. R. et al. Nanotechnology-enabled closed loop insulin delivery device: in vitro and in vivo evaluation of glucose-regulated insulin release for diabetes control. *Adv. Funct. Mater.* **21**, 73–82 (2011).
19. Gu, Z. et al. Injectable nano-network for glucose-mediated insulin delivery. *ACS nano* **7**, 4194–4201 (2013).
20. Chai, Z., Ma, L., Wang, Y. & Ren, X. Phenylboronic acid as a glucose-responsive trigger to tune the insulin release of glycopolymer nanoparticles. *J. Biomater. Sci. Polym. Ed.* **27**, 599–610 (2016).
21. Ma, R. & Shi, L. Phenylboronic acid-based glucose-responsive polymeric nanoparticles: synthesis and applications in drug delivery. *Polym. Chem.* **5**, 1503–1518 (2014).
22. Shiino, D. et al. Amine containing phenylboronic acid gel for glucose-responsive insulin release under physiological pH. *J. Control. Release* **37**, 269–276 (1995).
23. GhavamiNejad, A., Lu, B., Giacca, A. & Wu, X. Y. Glucose regulation by modified boronic acid-sulfobetaine zwitterionic nanogels - a non-hormonal strategy for the potential treatment of hyperglycemia. *Nanoscale* **11**, 10167–10171 (2019).
24. Wang, J. Q. et al. Charge-switchable polymeric complex for glucose-responsive insulin delivery in mice and pigs. *Sci. Adv.* **5**, eaaw4357 (2019).
25. Zhang, C., Lu, X. L., Wang, Z. H. & Xia, H. S. Progress in utilizing dynamic bonds to fabricate structurally adaptive self-healing, shape memory, and liquid crystal polymers. *Macromol. Rapid Comm.* **43**, 2100768 (2022).
26. Oh, J. Y. et al. Stretchable self-healable semiconducting polymer film for active-matrix strain-sensing array. *Sci. Adv.* **5**, eaav3097 (2019).
27. Vatankhah-Varnoosfaderani, M., Hashmi, S., GhavamiNejad, A. & Stadler, F. J. Rapid self-healing and triple stimuli responsiveness of a supramolecular polymer gel based on boron-catechol interactions in a novel water-soluble mussel-inspired copolymer. *Polym. Chem.* **5**, 512–523 (2014).
28. Xu, X. Y. et al. Bioadhesive hydrogels demonstrating pH-independent and ultrafast gelation promote gastric ulcer healing in pigs. *Sci. Transl. Med.* **12**, eaba8014 (2020).
29. Jia, Y. et al. Hydrogel dressing integrating FAK inhibition and ROS scavenging for mechano-chemical treatment of atopic dermatitis. *Nat. Commun.* **14**, 2478 (2023).
30. Hu, S. et al. A mussel-inspired film for adhesion to wet buccal tissue and efficient buccal drug delivery. *Nat. Commun.* **12**, 1689 (2021).
31. Faure, E. et al. Catechols as versatile platforms in polymer chemistry. *Prog. Polym. Sci.* **38**, 236–270 (2013).
32. GhavamiNejad, A., Park, C. H. & Kim, C. S. In situ synthesis of antimicrobial silver nanoparticles within antifouling Zwitterionic hydrogels by catecholic redox chemistry for wound healing application. *Biomacromolecules* **17**, 1213–1223 (2016).
33. Gao, J. J., Xing, F. F., Bai, Y. L. & Zhu, S. R. Synthesis, spectroscopy, and binding constants of ketocatechol-containing iminodiacetic acid and its Fe(III), Cu(II), and Zn(II) complexes and reaction of Cu(II) complex with H2O2 in aqueous solution. *Dalton Trans.* **43**, 7964–7978 (2014).
34. Xu, Z. P. Mechanics of metal-catecholate complexes: the roles of coordination state and metal types. *Sci. Rep.* **3**, 2914 (2013).
35. Gan, D. et al. Plant-inspired adhesive and tough hydrogel based on Ag-Lignin nanoparticles-triggered dynamic redox catechol chemistry. *Nat. Commun.* **10**, 1487 (2019).
36. Kang, T. et al. Formation, removal, and reformation of surface coatings on various metal oxide surfaces inspired by mussel adhesives. *ACS Appl. Mater. Inter* **7**, 24656–24662 (2015).
37. Yuan, C. et al. Protein-responsive assemblies from catechol-metal ion supramolecular coordination. *Soft Matter* **11**, 2243–2250 (2015).
38. GhavamiNejad, A., Ashammakhi, N., Wu, X. Y. & Khademhosseini, A. Crosslinking strategies for three-dimensional bioprinting of polymeric hydrogels. *Small* **16**, e2002931 (2020).
39. Kim, S. et al. In situ mechanical reinforcement of polymer hydrogels via metal-coordinated crosslink mineralization. *Nat. Commun.* **12**, 667 (2021).
40. Suzuki, Y. et al. Reactivity of boronic acids toward catechols in aqueous solution. *J. Org. Chem.* **85**, 5255–5264 (2020).
41. GhavamiNejad, A. et al. Mussel-inspired electrospun smart magnetic nanofibers for hyperthermic chemotherapy. *Adv. Funct. Mater.* **25**, 2867–2875 (2015).
42. Nakahata, M. et al. pH- and sugar-responsive gel assemblies based on boronate-catechol interactions. *ACS Macro Lett.* **3**, 337–340 (2014).
43. Asha, A. B. et al. Dopamine assisted self-cleaning, antifouling, and antibacterial coating via dynamic covalent interactions. *ACS Appl Mater. Inter* **14**, 9557–9569 (2022).
44. Farinas, C. S., Bueno, S. M. A. & Miranda, E. A. Adsorption of glucagon and insulin on an immobilized metal ion affinity chromatography silica matrix. *Adsorpt. Sci. Technol.* **21**, 883–896 (2003).
45. Kushner, R. S., Lemli, L. & Smith, D. W. Zinc glucagon in the management of idiopathic hypoglycemia. *J. Pediatrics* **63**, 1111–1115 (1963).
46. Rosenbloom, A. L., Smith, D. W. & Cohan, R. C. Zinc glucagon in idiopathic hypoglycemia of infancy: efficacy in long-term control. *Am. J. Dis. Child.* **112**, 107–111 (1966).
47. Sokal, J. E. The duration of glucagon effect1. *Endocrinology* **67**, 774–783 (1960).
48. Liu, J. F. et al. Smart" matrix microneedle patch made of self-crosslinkable and multifunctional polymers for delivering insulin on-demand. *Adv. Sci.* **10**, 2303665 (2023).
49. Zhang, W. et al. Catechol-functionalized hydrogels: biomimetic design, adhesion mechanism, and biomedical applications. *Chem. Soc. Rev.* **49**, 433–464 (2020).
50. Yang, B. et al. Optimization of truncated glucagon peptides to achieve selective, high potency, full antagonists. *J. Med. Chem.* **64**, 4697–4708 (2021).
51. Ardalan, N., Mirzaie, S., Sepahi, A. A. & Khavari-Nejad, R. A. Novel mutant of Escherichia coli asparaginase II to reduction of the glutaminase activity in treatment of acute lymphocytic leukemia by molecular dynamics simulations and QM-MM studies. *Med. Hypotheses* **112**, 7–17 (2018).
52. Abraham, M. B. et al. ISPAD Clinical Practice Consensus Guidelines 2022: assessment and management of hypoglycemia in children and adolescents with diabetes. *Pediatr. Diabetes* **23**, 1322–1340 (2022).
53. Liu, P., Kim, B., Friesner, R. A. & Berne, B. J. Replica exchange with solute tempering: A method for sampling biological systems in explicit water. *Proc. Natl. Acad. Sci.* **102**, 13749–13754 (2005).
54. Berg, B. A. & Neuhaus, T. Multicanonical algorithms for first order phase transitions. *Phys. Lett. B* **267**, 249–253 (1991).
55. Sugita, Y. & Okamoto, Y. Replica-exchange multicanonical algorithm and multicanonical replica-exchange method for simulating systems with rough energy landscape. *Chem. Phys. Lett.* **329**, 261–270 (2000).

56. Stolovitzky, G. & Berne, B. Catalytic tempering: A method for sampling rough energy landscapes by Monte Carlo. *Proc. Natl Acad. Sci.* **97**, 11164–11169 (2000).
57. Taweechat, P., Pandey, R. B. & Sompornpisut, P. Conformation, flexibility and hydration of hyaluronic acid by molecular dynamics simulations. *Carbohydr. Res.* **493**, 108026 (2020).
58. Aoki, T. T. Glucagon, Part 1 (Handbook of Experimental Pharmacology). *Springer Verlag* **66** (1983).
59. Trading, F., Nielsen, P., Pingel, M. & Vølund, A. A. Biological and chemical properties of two glucagon preparations with prolonged action. *Eur. J. Pharmacol.* **7**, 206–210 (1969).
60. Sasaki, K., Dockerill, S., Adamiak, D. A., Tickle, I. J. & Blundell, T. X-ray analysis of glucagon and its relationship to receptor binding. *Nature* **257**, 751–757 (1975).
61. Release, S. Maestro-Desmond Interoperability Tools. (Schrödinger, 2017).
62. Mark, P. & Nilsson, L. Structure and dynamics of the TIP3P, SPC, and SPC/E water models at 298 K. *J. Phys. Chem. A* **105**, 9954–9960 (2001).
63. Banks, J. L. et al. Integrated modeling program, applied chemical theory (IMPACT). *J. Comput. Chem.* **26**, 1752–1780 (2005).
64. Wang, L., Friesner, R. A. & Berne, B. Replica exchange with solute scaling: a more efficient version of replica exchange with solute tempering (REST2). *J. Phys. Chem. B* **115**, 9431–9438 (2011).
65. Dennington, R., Keith, T. A. & Millam, J. M. GaussView, version 6.0. 16. *Semichem Inc Shawnee Mission KS* (2016).
66. Bochevarov, A. D. et al. Jaguar: A high-performance quantum chemistry software program with strengths in life and materials sciences. *Int. J. Quantum Chem.* **113**, 2110–2142 (2013).

Acknowledgements

The work was supported through funding from The Leona M. & Harry B. Helmsley Charitable Trust Grant #2109-04810, Natural Sciences and Engineering Research Council of Canada (NSERC) Equipment grants (EQPEQ 374799-09; EQPEQ 440689-13) to X.Y.W. The authors would also like to thank Ontario Graduate Scholarship and University of Toronto Open scholarships to B.L. and J.F.L., the NSERC CREATE ContRoL scholarship and Pfizer Canada Graduate Fellowship in Pharmaceutical Sciences to S.M., the Mitacs Accelerate Internship to JFL and SM, the NSERC CREATE ContRoL and Best and Banting Diabetes Centre travel wards to J.F.L., the staff of the Analytical Laboratory for Environmental Science Research (ANALEST), Centre for Research and Applications in Fluidic Technologies (CRAFT), and Microscopy Imaging Laboratory (MIL) facilities at the University of Toronto for helping with analytical experiments.

Author contributions

Project conceptualization and design: Amin GhavamiNejad (A.GN.), and X.Y.W.; Polymer synthesis, microneedle patch fabrication, and characterization: A.GN., J.F.L.; In vitro testing: A.GN., J.F.L., B.L., and M.S.; Molecular Dynamics simulations: S.M.; Data analysis: A.GN., J.F.L., B.L., S.M., A.G., and X.Y.W.; In vivo testing: A.GN., J.F.L., B.L., S.M., and M.S.; Supervision of in vivo study: A.G. Manuscript writing: A.GN., with revisions and input from all authors.

Competing interests

A patent application (PCT/CT2023/051373) related to this work has been filed by the authors (Xiao Yu Wu, Amin GhavamiNejad, Jackie Fule Liu, Brian Lu, Adria Giacca, Sako Mirzaie, and Melisa Samarikhalaj). The authors have no other competing interests.

Additional information

Supplementary information The online version contains supplementary material available at https://doi.org/10.1038/s41467-025-58278-4.

Correspondence and requests for materials should be addressed to Xiao Yu Wu.

Peer review information *Nature Communications* thanks Qian Chen, Hao Dong, and the other, anonymous, reviewer(s) for their contribution to the peer review of this work. A peer review file is available.